

Phase field modelling of precipitate morphologies in systems with tetragonal interfacial free energy anisotropy

Arijit Roy and M. P. Gururajan*

Department of Metallurgical Engineering and Materials Science, Indian Institute of Technology Bombay, Powai, Mumbai 400076 INDIA.

ARTICLE HISTORY

July 2017

ABSTRACT

A wide variety of morphologies arise due to the tetragonal anisotropy in interfacial free energy. In this paper, we report on a family of Extended Cahn-Hilliard (ECH) models for incorporating tetragonal anisotropy in interfacial free energy. We list the non-zero and independent parameters that are introduced in our model and list the constraints on them. For appropriate choice of these parameters, our model can produce a many of the morphologies seen in tetragonal systems such as dipyrramids, rods, plates and their truncated variants. We analyse these morphologies and show that they indeed are equilibrium morphologies consistent with the Wulff construction.

KEYWORDS

phase field modelling, faceted precipitates, interfacial energy anisotropy, tetragonal anisotropy, Wulff plot

1. Introduction

A wide variety of precipitate and crystalline morphologies are reported in tetragonal systems, during phase transformations and crystal growth, respectively. The physiochemical properties of such particles depends on their morphologies; for example, in the case of TiO_2 , the properties of the crystallites can be tuned by engineering its facets [1]; and, in the case of tin oxide whiskers, the gas sensing properties differ depending on the morphology [2]. Hence, understanding the formation of such faceted morphologies is of great interest both from a scientific and application point of view.

In some cases, such as partially stabilized ZrO_2 and tetragonal ZrO_2 precipitates in cubic ZrO_2 solid solution [3], and Cu precipitates in Fe-Cu system [4, 5], the elastic energy plays a key role (apart from the tetragonal crystal structure of the systems). However, we do not consider the elastic stress effects in this paper (though, our model can be extended to include the elastic stress effects).

On the other hand, even in the absence of elastic stresses, the interphase interfacial free energy anisotropy that arises from the tetragonal crystal structure of the participating phases could be important in determining the crystallite / precipitate / second phase morphologies; see for example, metallic whiskers of β -Sn [6–8]; PdO formed by

*Corresponding author. Email: gururajan.mp@gmail.com

internal oxidation of Pd in SiO₂ [9]; single crystal PbTiO₃ nanorods synthesised by solid state reaction [10]; SnO₂ nano plates obtained using hydrothermal oxidation of SnS₂ [11]; SnO thin plates obtained using oxidation in an aqueous solution [12] and plasma processing [13]; faceted, short Sn whiskers grown on Sn finish surfaces [14]; faceted morphology of In crystallites deposited on cleaved graphite surface [15] and on potassium chloride [16]; tetragonal nano-rods and nano-tubes with cubic cross-section in α -MnO₂ synthesised via the hydrothermal route [17]; and, faceted, tetragonal CeO₂ nanocrystals obtained via the hydrothermal synthesis [18]. Specifically, the studies on tetragonal TiO₂ deserve special mention; a wide variety of morphologies such as tetragonal di-pyramids and their truncated versions are predicted based on interfacial free energy calculations (at times based on first principle calculations) and faceted nanorods, plates, di-pyramids and their truncated versions are obtained experimentally [1, 19–21].

Further, it is known that during solid-solid phase transformations, the relative crystalline symmetry of the phases determines the symmetry of the interface [22, 23]; for example, if the phases are $L1_2$ -ordered (FCC derivative structure), the antiphase boundaries reflect tetragonal symmetry [23]. Thus, even in non-tetragonal crystal systems, the interfacial free energy can have tetragonal symmetry.

Our aim in this paper is to study the morphology of precipitates in systems with tetragonal interfacial free energy anisotropy – using phase field models. Phase field models are ideal for the study of morphology of precipitates and crystallites; recently, we have used the Extended Cahn-Hilliard (ECH) model to study the precipitate morphologies in systems with cubic and hexagonal interfacial free energy anisotropy [24–26]. Some aspects of the tetragonal symmetry (distinction between c and a,b axes) can be introduced using the classical Cahn-Hilliard equation with second rank gradient free energy coefficient; and ECH models are not necessary [27–29]. However, using such second rank tensors, it is not possible to obtain some of the tetragonal morphologies observed in the experiments such as plates and rods with square cross-section, bi-pyramids and their truncated versions. Hence, in this paper, we use the ECH model for systems with tetragonal interfacial free energy anisotropy and show that our phase field model can indeed produce crystalline morphologies observed / predicted in these systems.

2. Formulation

In this paper, we briefly describe the ECH model [24, 25, 30, 31] to study the morphological evolution of precipitates in systems with tetragonal interfacial free energy anisotropy; the detailed formulation can be found elsewhere [26]. Our description is based on a scalar, compositional order parameter (c); however, the extension to non-conserved order parameters and to combinations of conserved and non-conserved order parameters is straightforward.

Let us consider a binary alloy with composition c ; we define the the gradient c_i (a vector), curvature c_{ij} (a second rank tensor) and aberration c_{ijk} (a third rank tensor) of the (scalar) composition field as follows: $c_i = \frac{\partial c}{\partial x_i}$; $c_{ij} = \frac{\partial^2 c}{\partial x_i \partial x_j}$; $c_{ijk} = \frac{\partial^3 c}{\partial x_i \partial x_j \partial x_k}$.

The free energy F , can be written as follows [26]:

$$F = N_V \int_V f dV, \quad (1)$$

where N_V is the number of atoms / molecules in the given volume V and f is the free energy density given by

$$\begin{aligned} f &= f_0(c) + P_{ij}^I c_i c_j + M_{ijkl}^I c_i c_j c_k c_l + Q_{ijkl}^{II} c_i c_j c_k c_l \\ &+ N_{ijklmn}^I c_i c_j c_k c_l c_m c_n + R_{ijklmn}^I c_i c_j c_k c_l c_m c_n, \end{aligned} \quad (2)$$

where, $P_{ij}^I = \frac{1}{2!} \frac{\partial^2 f}{\partial c_i \partial c_j} \Big|_{c_0}$ is a second rank (coefficient) tensor; $M_{ijkl}^I = \frac{1}{4!} \frac{\partial^4 f}{\partial c_i \partial c_j \partial c_k \partial c_l} \Big|_{c_0}$ and $Q_{ijkl}^{II} = \frac{1}{2!} \frac{\partial^2 f}{\partial c_{ij} \partial c_{kl}} \Big|_{c_0}$ are fourth rank (coefficient) tensors; and, $N_{ijklmn}^I = \frac{1}{6!} \frac{\partial^6 f}{\partial c_i \partial c_j \partial c_k \partial c_l \partial c_m \partial c_n} \Big|_{c_0}$, $N_{ijklmn}^{II} = \frac{1}{5!} \frac{\partial^5 f}{\partial c_{ij} \partial c_k \partial c_l \partial c_m \partial c_n} \Big|_{c_0}$, and, $R_{ijklmn}^I = \frac{1}{2!} \frac{\partial^2 f}{\partial c_{ijk} \partial c_{lmn}} \Big|_{c_0}$ are the sixth rank (coefficient) tensors.

In writing the above expression, we have assumed that there are no elastic stresses and that the underlying crystalline continuum is centrosymmetric; we have used Gauss theorem and positive-definiteness arguments; the details of the derivation is similar to that of ECH for systems with cubic [30, 31] and hexagonal [24, 25] symmetries and can be found in [26].

As described by Nye in his classic text [32], using intrinsic symmetries (such as, for sufficiently smooth f , $\frac{\partial^2 f}{\partial c_i \partial c_j} = \frac{\partial^2 f}{\partial c_j \partial c_i}$) and commutative properties (such as $c_i c_j = c_j c_i$), it is possible to reduce the number of independent components of the various tensors. Specifically, we can reduce the independent components of P_{ij}^I from 9 to 6, that of M_{ijkl}^I from 81 to 15, that is Q_{ijkl}^{II} from 81 to 21, that of N_{ijklmn}^I from 729 to 28, and, that of R_{ijklmn}^I from 729 to 55 (see below for the enumeration for sixth rank tensors).

It is easier to identify and enumerate the independent components and their numbers, respectively, for the fourth and sixth rank tensors if we represent them in the reduced matrix notation. Such notation, known as Voigt notation (represented as matrices) is available in Nye for fourth rank tensors; here we show a similar notation for sixth rank tensors.

Since both N_{ijklmn}^I and R_{ijklmn}^I are invariant under the exchange of i, j and k , or l, m and n indices, we collect all possible independent ways in which i, j and k indices can appear and reduce them to a single index as follows:

$$\begin{aligned} 111 &\rightarrow 1 & 222 &\rightarrow 4 & 333 &\rightarrow 7 & 123 &\rightarrow 0. \\ 221 &\rightarrow 2 & 112 &\rightarrow 5 & 113 &\rightarrow 8 & & \\ 331 &\rightarrow 3 & 332 &\rightarrow 6 & 223 &\rightarrow 9 & & \end{aligned} \quad (3)$$

Since each pair of ijk -indices can be arranged in 10 independent ways, a sixth rank tensor with two such pair of indices, can be expressed in a 10×10 matrix form.

Thus, we can write N_{ijklmn}^I in $N_{\alpha\beta}^I$ (or similarly R_{ijklmn}^I in $R_{\alpha\beta}^I$) form as follows:

$$\begin{bmatrix} N_{11}^I & N_{12}^I & N_{13}^I & N_{14}^I & N_{15}^I & N_{16}^I & N_{17}^I & N_{18}^I & N_{19}^I & N_{10}^I \\ \bullet & N_{22}^I & N_{23}^I & N_{24}^I & N_{25}^I & N_{26}^I & N_{27}^I & N_{28}^I & N_{29}^I & N_{20}^I \\ \bullet & \bullet & N_{33}^I & N_{34}^I & N_{35}^I & N_{36}^I & N_{37}^I & N_{38}^I & N_{39}^I & N_{30}^I \\ \bullet & \bullet & \bullet & N_{44}^I & N_{45}^I & N_{46}^I & N_{47}^I & N_{48}^I & N_{49}^I & N_{40}^I \\ \bullet & \bullet & \bullet & \bullet & N_{55}^I & N_{56}^I & N_{57}^I & N_{58}^I & N_{59}^I & N_{50}^I \\ \bullet & \bullet & \bullet & \bullet & \bullet & N_{66}^I & N_{67}^I & N_{68}^I & N_{69}^I & N_{60}^I \\ \bullet & \bullet & \bullet & \bullet & \bullet & \bullet & N_{77}^I & N_{78}^I & N_{79}^I & N_{70}^I \\ \bullet & \bullet & \bullet & \bullet & \bullet & \bullet & \bullet & N_{88}^I & N_{89}^I & N_{80}^I \\ \bullet & \bullet & \bullet & \bullet & \bullet & \bullet & \bullet & \bullet & N_{99}^I & N_{90}^I \\ \bullet & \bullet & \bullet & \bullet & \bullet & \bullet & \bullet & \bullet & \bullet & N_{00}^I \end{bmatrix}$$

The lower diagonal components satisfying intrinsic symmetry are represented by \bullet . Thus, the total number of independent components (of N_{ijklmn}^I and R_{ijklmn}) obtained by adding the diagonal and upper diagonal (as lower diagonal terms are numerically equal to upper diagonal terms by intrinsic symmetry) term of the 10×10 matrix is 55. The tensor N_{ijklmn}^I has an additional symmetry: it is invariant under the exchange of all the i, j, k, l, m and n ; since there are 27 such components which are invariant under the exchange of indices, the total number of independent components for N_{ijklmn}^I is $55 - 27 = 28$.

Crystalline symmetry arguments are very powerful in reducing the total number of non-zero components and independent components; see Nani and Gururajan [24] for isotropic, cubic and hexagonal systems. In this paper, we use the direct inspection method of Nye [32] (which is valid for all crystal classes except trigonal and hexagonal) to reduce the the total number of non-zero and independent components of the coefficient tensors assuming tetragonal symmetry.

The characteristic symmetry for the tetragonal system is 4-fold [32]. There are seven tetragonal crystal classes; in this paper, we present the results for the ditetragonal-dipyramidal crystal class (represented by the symbol $4/mmm$ in International Tables and by D_{4h} in Schoenflies). The Fig. 1 shows the choice of axes and the symmetry operations for $4/mmm$. There exist three predominant axes of symmetry; namely, two 2-fold axes of symmetry or diad axes and one 4-fold axis of symmetry or tetrad axis. Using these symmetry operations and demanding that the tensors remain invariant under these operations, the independent and non-zero components for various tensors can be deduced.

In the case of \mathbf{P}^I tensor, the only non-zero surviving components are P_{11}^I , P_{22}^I and P_{33}^I . Of these, there are only two independent components, namely, P_{11}^I and P_{33}^I . Let

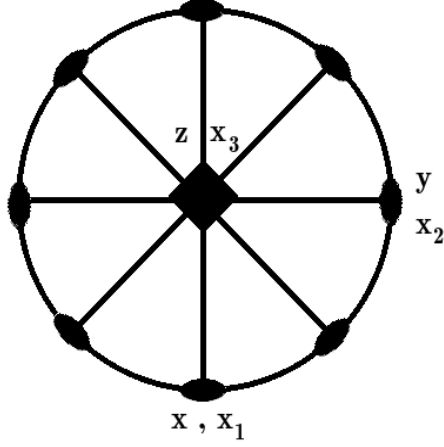


Figure 1. Choice of axes and the allowed symmetry operations for ditetragonal-dipyramidal crystal class ($4/mmm$).

us call these two components as p_1 and p_2 :

$$\begin{aligned} p_1 &= P_{11}^I = P_{22}^I \\ p_2 &= P_{33}^I \end{aligned} \quad (4)$$

The free energy contribution originating from the second rank gradient tensorial term can be obtained by the double contraction (two inner multiplications) $P_{ij}^I c_i c_j$. Let us call the resultant scalar as P^2 .

$$P^2 = p_1(c_1^2 + c_2^2) + p_2 c_3^2. \quad (5)$$

Thus, we have reduced our second rank tensor term of the free energy expansion into a polynomial in the gradient terms.

Similarly, the total number of independent components for a fourth rank coefficient tensor in systems with tetragonal symmetry is reduced to 6: $M_{11}^I, M_{33}^I, M_{44}^I, M_{66}^I, M_{12}^I$, and, M_{13}^I . The fourth rank curvature coefficient tensor Q_{ijkl}^{II} also has the same non-zero tensor components as M_{ijkl}^I . Similar to the case of second rank gradient tensor \mathbf{P}^I , we rename the independent and non-zero components of \mathbf{M}^I and \mathbf{Q}^{II} as listed in Table. 1.

Table 1. Independent and non-zero components of fourth rank gradient tensor \mathbf{M}^I and curvature tensor \mathbf{Q}^{II} .

Components	for \mathbf{M}^I	for \mathbf{Q}^{II}
$M_{11}^I = M_{22}^I$	m_1	q_1
M_{33}^I	m_2	q_2
$M_{12}^I (\equiv M_{21}^I)$	m_3	q_3
$M_{13}^I = M_{23}^I (\equiv M_{31}^I, M_{32}^I)$	m_4	q_4
$M_{44}^I = M_{55}^I$	m_5	q_5
M_{66}^I	m_6	q_6

Given the independent and non-zero components of these tensors, it is straightforward to obtain the free energy contributions stemming from the inner products $M_{ijkl}^I c_i c_j c_k c_l$ (say, P^4) and $Q_{ijkl}^{II} c_{ij} c_{kl}$ (say, Q) in Eq. 2; this results in the polynomial form as follows (see Table 2 for the detailed enumeration).

$$\begin{aligned}
P^4 &= m_1(c_1^4 + c_2^4) + m_2c_3^4 \\
&+ 2m_3c_1^2c_2^2 + 2m_4c_3^2(c_1^2 + c_2^2) \\
&+ m_5c_3^2(c_1^2 + c_2^2) + m_6c_1^2c_2^2.
\end{aligned} \tag{6}$$

Note that the factors of 2 come from the symmetry of the matrix (off diagonal terms on the lower half of the matrix form). Clubbing the coefficients for $c_1^2c_2^2$ and $c_3^2(c_1^2 + c_2^2)$, we can rewrite Eq. 6 as follows:

$$\begin{aligned}
P^4 &= m_1(c_1^4 + c_2^4) + m_2c_3^4 \\
&+ (2m_3 + m_6)c_1^2c_2^2 + (2m_4 + m_5)c_3^2(c_1^2 + c_2^2).
\end{aligned} \tag{7}$$

Thus, without loss of generality, we can assume that there are only four constants are needed for \mathbf{M}^I ; the terms m_3 and m_6 and m_4 and m_5 can be clubbed together; to keep the notation simple, we use m_3 to denote $2m_3 + m_6$ and m_4 to denote $2m_4 + m_5$; thus, we obtain

$$P^4 = m_1(c_1^4 + c_2^4) + m_2c_3^4 + m_3c_1^2c_2^2 + m_4c_3^2(c_1^2 + c_2^2). \tag{8}$$

$$\begin{aligned}
Q &= q_1(c_{11}^2 + c_{22}^2) + q_2c_{33}^2 \\
&+ 2q_3c_{11}c_{22} + 2q_4(c_{11} + c_{22})c_{33} \\
&+ q_5(c_{13}^2 + c_{23}^2) + q_6c_{12}^2.
\end{aligned} \tag{9}$$

As opposed to \mathbf{M}^I , we need all the six constants for \mathbf{Q} which is a consequence of the lower intrinsic symmetry of \mathbf{Q} , namely, all possible exchanges of the indices are not allowed.

Table 2. Listing of c -derivatives that multiply \mathbf{M}^I and \mathbf{Q}^{II} tensor coefficients.

Component of \mathbf{M}^I	Corresponding c -derivatives	Component of \mathbf{Q}^I	Corresponding c -derivatives
m_1	c_1^4 c_2^4	q_1	c_{11}^2 c_{22}^2
m_2	c_3^4	q_2	c_{33}^2
m_3	$c_1^2c_2^2$	q_3	$c_{11}c_{22}$
m_4	$c_1^2c_3^2$ $c_2^2c_3^2$	q_4	$c_{11}c_{33}$ $c_{22}c_{33}$
m_5	$c_2^2c_3^2$ $c_1^2c_3^2$	q_5	$c_{23}c_{23}$ $c_{13}c_{13}$
m_6	$c_1^2c_2^2$	q_6	$c_{12}c_{12}$

The sixth rank tensor \mathbf{N}^I is reduced to the form shown in Table 3, and, the non-zero and independent components of the sixth rank tensorial coefficient are listed in

Table. 4. The non-zero and independent components of $\mathbf{R}^{\mathbf{I}}$ are same as $\mathbf{N}^{\mathbf{I}}$ tensor. Thus, after employing the crystalline symmetry arguments, we are able to reduce the independent components of $\mathbf{N}^{\mathbf{I}}$ and $\mathbf{R}^{\mathbf{I}}$ tensors from 55 to 11.

Table 3. Non-zero and independent components of the sixth rank tensor $\mathbf{N}^{\mathbf{I}}$ in matrix form.

$$\mathbf{N}^{\mathbf{I}} = \left[\begin{array}{cccccc} N_{11}^{\mathbf{I}} & N_{12}^{\mathbf{I}} & N_{13}^{\mathbf{I}} & & & \\ \bullet & N_{22}^{\mathbf{I}} & N_{23}^{\mathbf{I}} & & & \\ \bullet & \bullet & N_{33}^{\mathbf{I}} & & & \\ & & & N_{11}^{\mathbf{I}} & N_{12}^{\mathbf{I}} & N_{13}^{\mathbf{I}} \\ & & & \bullet & N_{22}^{\mathbf{I}} & N_{23}^{\mathbf{I}} \\ & & & \bullet & \bullet & N_{33}^{\mathbf{I}} \\ & & & & & & N_{77}^{\mathbf{I}} & N_{78}^{\mathbf{I}} & N_{78}^{\mathbf{I}} \\ & & & & & & \bullet & N_{88}^{\mathbf{I}} & N_{89}^{\mathbf{I}} \\ & & & & & & \bullet & \bullet & N_{88}^{\mathbf{I}} \\ & & & & & & & & & N_{00}^{\mathbf{I}} \end{array} \right]$$

Table 4. Independent and non-zero components of sixth rank gradient tensor $\mathbf{N}^{\mathbf{I}}$ and curvature tensor $\mathbf{R}^{\mathbf{I}}$.

Components	for $\mathbf{N}^{\mathbf{I}}$	for $\mathbf{R}^{\mathbf{I}}$	Components	for $\mathbf{N}^{\mathbf{I}}$	for $\mathbf{R}^{\mathbf{I}}$
$N_{11}^{\mathbf{I}} = N_{44}^{\mathbf{I}}$	n_1	r_1	$N_{77}^{\mathbf{I}}$	n_2	r_2
$N_{22}^{\mathbf{I}} = N_{55}^{\mathbf{I}}$	n_3	r_3	$N_{89}^{\mathbf{I}}$	n_4	r_4
$N_{13}^{\mathbf{I}} = N_{46}^{\mathbf{I}}$	n_5	r_5	$N_{23}^{\mathbf{I}} = N_{56}^{\mathbf{I}}$	n_6	r_6
$N_{88}^{\mathbf{I}} = N_{99}^{\mathbf{I}}$	n_7	r_7	$N_{33}^{\mathbf{I}} = N_{66}^{\mathbf{I}}$	n_8	r_8
$N_{78}^{\mathbf{I}} = N_{79}^{\mathbf{I}}$	n_9	r_9	$N_{12}^{\mathbf{I}} = N_{45}^{\mathbf{I}}$	n_{10}	r_{10}
$N_{00}^{\mathbf{I}}$	n_{11}	r_{11}			

We obtain the scalar contribution to the free energy from the two sixth rank tensorial coefficients $N_{ijklmn}^{\mathbf{I}}$ and $R_{ijklmn}^{\mathbf{I}}$ by the inner product of these tensors with the gradients ($c_i c_j c_k c_l c_m c_n$) and aberrations ($c_{ijk} c_{lmn}$) respectively. Let the free energy contribution originating from gradient term be called P^6 and that from aberration term be called as R . The detailed enumeration of these terms is shown in Table. 5.

Using Table. 5, we can easily build the free energy in polynomial form. To derive the sixth order gradient free energy polynomial (P^6), we multiply the elements of column

Table 5. Listing of c -derivatives that multiply \mathbf{N}^I and \mathbf{R}^I tensor coefficients.

Component of \mathbf{N}^I	Multiplied c -derivatives	Component of \mathbf{R}^I	Multiplied c -derivatives
n_1	c_1^6 c_2^6	r_1	c_{111}^2 c_{222}^2
n_2	c_3^6	r_2	c_{333}^2
n_3	$c_1^2 c_2^4$ $c_1^4 c_2^2$	r_3	c_{221}^2 c_{112}^2
n_4	$c_1^2 c_2^2 c_3^2$	r_4	$c_{113} c_{223}$
n_5	$c_1^4 c_3^2$ $c_2^4 c_3^2$	r_5	$c_{111} c_{331}$ $c_{222} c_{332}$
n_6	$c_1^2 c_2^2 c_3^2$ $c_1^2 c_2^2 c_3^2$	r_6	$c_{221} c_{331}$ $c_{112} c_{332}$
n_7	$c_1^4 c_3^2$ $c_2^4 c_3^2$	r_7	$c_{113} c_{113}$ $c_{223} c_{223}$
n_8	$c_1^2 c_3^4$ $c_2^2 c_3^4$	r_8	c_{331}^2 c_{332}^2
n_9	$c_1^2 c_3^4$ $c_2^2 c_3^4$	r_9	$c_{333} c_{113}$ $c_{333} c_{223}$
n_{10}	$c_1^4 c_2^2$ $c_1^2 c_2^4$	r_{10}	$c_{111} c_{221}$ $c_{222} c_{112}$
n_{11}	$c_1^2 c_2^2 c_3^2$	r_{11}	c_{123}^2

1 with those in 2 and sum all such terms:

$$\begin{aligned}
P^6 &= n_1 (c_1^6 + c_2^6) + n_2 c_3^6 \\
&+ 2n_{10} c_1^2 c_2^2 (c_1^2 + c_2^2) + 2n_5 c_3^2 (c_1^4 + c_2^4) + n_3 c_1^2 c_2^2 (c_1^2 + c_2^2) \\
&+ 4n_6 c_1^2 c_2^2 c_3^2 + n_8 c_3^4 (c_1^2 + c_2^2) + 2n_9 c_3^4 (c_1^2 + c_2^2) + n_7 c_3^2 (c_1^4 + c_2^4) \\
&+ 2n_4 c_1^2 c_2^2 c_3^2 + n_{11} c_1^2 c_2^2 c_3^2.
\end{aligned} \tag{10}$$

Clubbing the coefficients of $c_1^2 c_2^2 (c_1^2 + c_2^2)$, $c_3^2 (c_1^4 + c_2^4)$, $c_3^4 (c_1^2 + c_2^2)$ and $c_1^2 c_2^2 c_3^2$, we get

$$\begin{aligned}
P^6 &= n_1 (c_1^6 + c_2^6) + n_2 c_3^6 \\
&+ (2n_{10} + n_3) c_1^2 c_2^2 (c_1^2 + c_2^2) + (2n_5 + n_7) c_3^2 (c_1^4 + c_2^4) \\
&+ (n_8 + 2n_9) c_3^4 (c_1^2 + c_2^2) \\
&+ (4n_6 + 2n_4 + n_{11}) c_1^2 c_2^2 c_3^2.
\end{aligned} \tag{11}$$

Thus, without loss of generality, we can assume that six independent components are needed for \mathbf{N}^I .

Similarly, the aberration term R is written as follows:

$$\begin{aligned}
R = & r_1 (c_{111}^2 + c_{222}^2) + r_2 c_{333}^2 \\
& + 2r_{10} (c_{111}c_{221} + c_{222}c_{112}) + 2r_5 (c_{111}c_{331} + c_{222}c_{332}) \\
& + r_3 (c_{221}c_{221} + c_{112}c_{112}) + 2r_6 (c_{221}c_{331} + c_{112}c_{332}) \\
& + r_8 (c_{331}c_{331} + c_{332}c_{332}) + 2r_9 (c_{333}c_{113} + c_{333}c_{223}) \\
& + r_7 (c_{113}c_{113} + c_{223}c_{223}) + 2r_4 c_{113}c_{223} + r_{11} c_{123}c_{123}.
\end{aligned} \tag{12}$$

Thus, in contrast to $\mathbf{N}^{\mathbf{I}}$, we need eleven independent components to describe $\mathbf{R}^{\mathbf{I}}$.

Thus, we have managed to express the free energy in polynomial form in terms of the gradient, curvature and aberration components:

$$\begin{aligned}
f = & f_0 + P(c_1, c_2, c_3) + Q(c_{11}, c_{22}, c_{33}, c_{12}, c_{23}, c_{13}) \\
& + R(c_{111}, c_{222}, c_{333}, c_{112}, c_{113}, c_{221}, c_{223}, c_{331}, c_{332}, c_{123}),
\end{aligned} \tag{13}$$

where f_0 is the bulk free energy density (typically assumed to be a double well potential, namely, $Ac^2(1-c)^2$), and, P , Q and R are homogeneous polynomials; further, P consists of three parts: homogeneous polynomials of orders 2 (denoted by P^2), 4 (denoted by P^4) and 6 (denoted by P^6); Q and R are homogeneous polynomials of order 2. In Table 6, we list the forms of these polynomials. The coefficients of these polynomials are assumed to be constants, and, as indicated below, by choosing them appropriately, we incorporate the tetragonal anisotropy in interfacial energy.

Table 6. Polynomials P , Q and R .

Polynomial	Order	Form
P^2	2	$p_1(c_1^2 + c_2^2) + p_2c_3^2$
P^4	4	$m_1(c_1^4 + c_2^4) + m_2c_3^4 + 2m_3c_1^2c_2^2 + 2m_4(c_1^2 + c_2^2)c_3^2$
P^6	6	$n_1(c_1^2 + c_2^2)^3 + n_2c_3^6$ $+n_3(c_1^2 + c_2^2)(c_1^2c_2^2) + n_4(c_1^2 + c_2^2)^2c_3^2$ $+n_5(c_1^2 + c_2^2)c_3^4 + n_6c_1^2c_2^2c_3^2$
Q	2	$q_1(c_{11}^2 + c_{22}^2) + q_2c_{33}^2$ $+2q_3c_{11}c_{22} + 2q_4(c_{11} + c_{22})c_{33}$ $+q_5(c_{13}^2 + c_{23}^2) + q_6c_{12}^2$
R	2	$r_1(c_{111}^2 + c_{222}^2) + r_2c_{333}^2 + r_3(c_{112}^2 + c_{221}^2)$ $+2r_4c_{113}c_{223} + 2r_5(c_{111}c_{331} + c_{222}c_{332})$ $+2r_6(c_{112}c_{332} + c_{221}c_{331}) + r_7(c_{113}^2 + c_{223}^2)$ $+r_8(c_{331}^2 + c_{332}^2) + 2r_9c_{333}(c_{113} + c_{223})$ $+2r_{10}(c_{111}c_{221} + c_{222}c_{112}) + r_{11}c_{123}^2$

The polynomials P , Q and R represent the contribution of interfacial free energy; hence, we demand their term-wise positive definiteness. Such a demand helps us derive the constraints on the independent components. Once again, such an exercise for second and fourth rank tensors have been carried out in Nye [32] and we have extended the algebra to sixth rank tensors. The constraints on the independent constants for the various tensor coefficients are summarised in Table 7.

Table 7. Constraints on the coefficients of the polynomials listed in Table 6: tetragonal anisotropy.

Tetragonal	
P^2	$p_1, p_2 \geq 0$
P^4	$m_1 \geq 0; m_2 \geq 0$ $m_3 \geq m_1 ; m_4 \geq \sqrt{m_2(m_1 + m_3)} $
P^6	$n_1 \geq 0; n_2 \geq 0; n_3 \geq 0; n_4 \geq 0;$ $n_5 \leq \sqrt{\frac{1}{2}n_2n_4} ; n_6 \leq n_4;$
Q	$q_1 \geq 0; q_2 \geq 0; q_5 \geq 0; q_6 \geq 0$ $q_3 \geq q_1 ; q_4 \geq \sqrt{q_2(q_1 + q_3)} $
R	$r_1 \geq 0; r_2 \geq 0; r_3 \geq 0; r_7 \geq 0; r_8 \geq 0; r_{11} \geq 0$ r_5 and r_6 should have same sign; $r_4 \leq r_7; r_9 \leq \sqrt{\frac{1}{2}r_2(r_4 + r_7)} $ $r_{10} \leq \sqrt{r_1r_3} ; r_{10}r_5r_6 \geq \frac{1}{2} [r_3(r_5)^2 + r_1(r_6)^2]$ $r_{12} = r_1; r_{13} = r_3; r_{14} = r_{10}$

2.1. Integrity basis and polynomial form

Nani and Gururajan [24] show that the polynomials in gradients can be directly written down using the integrity basis approach of Smith et al [33] for any of the 32 crystal classes – using the building blocks of these polynomials called integrity basis. However, for the higher order polynomials composed of curvature terms ($c_{ij}c_{kl}$), or the polynomials composed of aberration terms ($c_{ijk}c_{lmn}$), there is no integrity basis and our approach outlined above is to be used. As an example, we show the formulation of the P^4 polynomial using the integrity basis approach; more details of the approach and the formulation of the P^6 polynomial can be found in [26].

Let us consider the tetragonal-ditetragonal-dipyramidal crystal class. From Smith et al [33], the integrity bases are as follows: $c_1^2 + c_2^2$, c_3^2 and $c_1^2c_2^2$. For the fourth order gradient contribution, then, the free energy polynomial is given as

$$\begin{aligned}
 P^4 &= m'_1(c_1^2 + c_2^2)^2 + m'_2c_3^4 + m'_3c_1^2c_2^2 + m'_4(c_1^2 + c_2^2)c_3^2 \\
 &= m'_1(c_1^4 + c_2^4) + m'_2c_3^4 + (2m'_1 + m'_3)c_1^2c_2^2 + m'_4(c_1^2 + c_2^2)c_3^2, \quad (14)
 \end{aligned}$$

where m'_1 , m'_2 , m'_3 and m'_4 are the coefficients of the free energy polynomial. By comparing Eq. 8 with Eq. 14, we can see the following relationships:

$$\begin{aligned}
 m'_1 &= m_1 & 2m'_1 + m'_3 &= m_3 \\
 m'_2 &= m_2 & m'_4 &= m_4
 \end{aligned}$$

As m'_1 , m'_2 and m'_4 are equal to m_1 , m_2 and m_4 respectively, constraints are also identical to non-primed components. Further, knowing the constraint on m'_1 and m_3 , we can obtain the constraint on m'_3 .

Similarly, we can build the sixth order polynomial in tetragonal symmetry.

2.2. Anisotropy of the higher order polynomials

As indicated elsewhere (Roy et al [25] and Roy [26]), by plotting the polynomials listed in Table. 6 (after normalising – in real space in the case of polynomials based on gradients and in reciprocal space in the case of polynomials based on curvature and aberration terms – with the primes indicating normalisation) for various choices of the parameters, the anisotropy that would be incorporated for the given parameters can be better understood. Note that though these polynomials are built by considering the symmetry of the free energy, they are also useful in describing any direction dependent property.

For example, for the choice of $m_1 = 1.0$, $m_2 = 1.5$, $m_3 = 2$ and $m_4 = 0.3$ the polar plot is as shown in Fig. 2 (a) – indicating a preference of $\langle 100 \rangle$ plane over $\langle 110 \rangle$. Similarly, to make $\langle 110 \rangle$ planes favourable, we use $m_1 = 1.2$, $m_2 = 1.5$, $m_3 = 0.2$ and $m_4 = 0.1$ and resulting polar plot is shown in Fig. 2 (b).

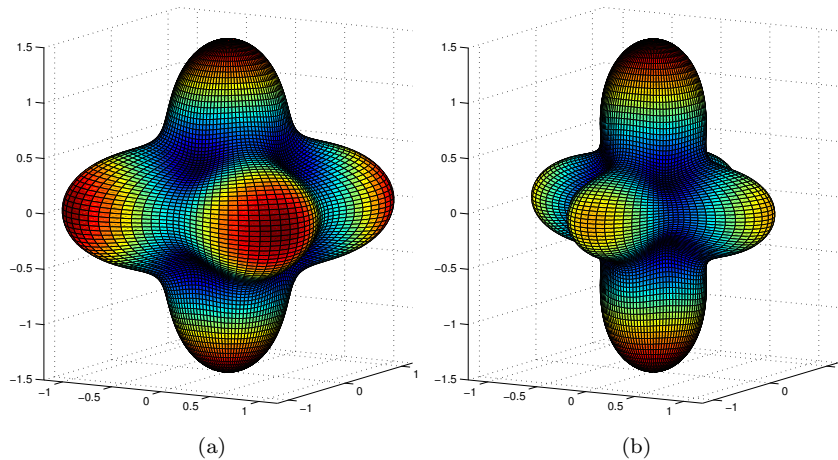


Figure 2. 3-D polar plots in a tetragonal anisotropic system obtained using $[P^4]'$. The choice of the polynomial coefficients are such that either (a) $\langle 100 \rangle$ planes or (b) $\langle 111 \rangle$ planes are the preferred planes.

If we choose $m_1 = 2.0$, $m_2 = 3$, $m_3 = -1.4$ and $m_4 = 0.9$, we can see in Fig. 3 (a), that there is no minima along the z -direction and hence $\langle 001 \rangle$ planes will not be present. Fig. 3 (b) shows the xy -section of the 3-D polar plot and one can clearly see the four fold symmetry. In Fig. 3 (c), the xz -section is shown, which has a dip in the xy plane. From these three plots, if we imagine the equilibrium shape of the precipitate, we can easily see that it leads to a tetragonal prism. Similarly, if we choose $m_1 = 2.0$, $m_2 = 0.1$, $m_3 = -1.5$ and $m_4 = 1.0$, we can obtain a dip along the z -direction and hence $\langle 001 \rangle$ planes will form in the precipitate morphology. We show the 3-D polar plot, xy and xz -sections in Fig. 4 (a), (b) and (c) respectively. We can see that the equilibrium shape of the precipitate that results from these polar plots and their sections is a tetragonal plate like morphology.

The polynomial $[P^4]'$ lacks $c_1^2 c_2^2 c_3^2$ and hence we can not control the energetics of $\langle 100 \rangle$ and $\langle 111 \rangle$ planes simultaneously. Using (normalised version of) Eq. 11 and with the choice of $n_1 = 0.5$, $n_2 = 2.0$, $n_3 = 5.0$, $n_4 = 14.0$, $n_5 = 1.0$ and $n_6 = -60.0$ we obtain the polar plot as shown in Fig. 5 (a). In this case we can see that, $\langle 100 \rangle$ and $\langle 111 \rangle$ planes can simultaneously form in the equilibrium precipitate morphology. On the other hand, if we choose $n_1 = 1.0$, $n_2 = 0.27$, $n_3 = 5.0$, $n_4 = 10$, $n_5 = 6$ and $n_6 = -59.0$, as shown in Fig. 5 (b), $\langle 100 \rangle$, $\langle 001 \rangle$ and $\langle 111 \rangle$ planes can simultaneously develop in the equilibrium precipitate morphology.

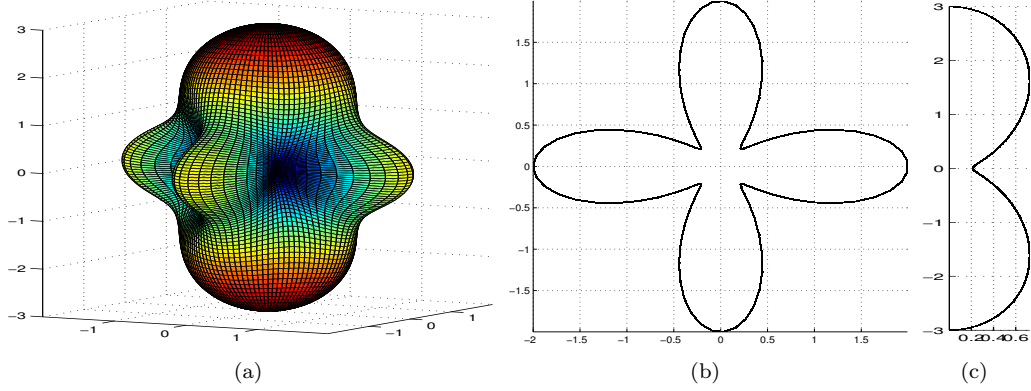


Figure 3. (a) 3-D polar plot along with (b) xy and (c) xz sections in a tetragonal anisotropic system for prism like equilibrium morphology; obtained using $[P^4]'$.

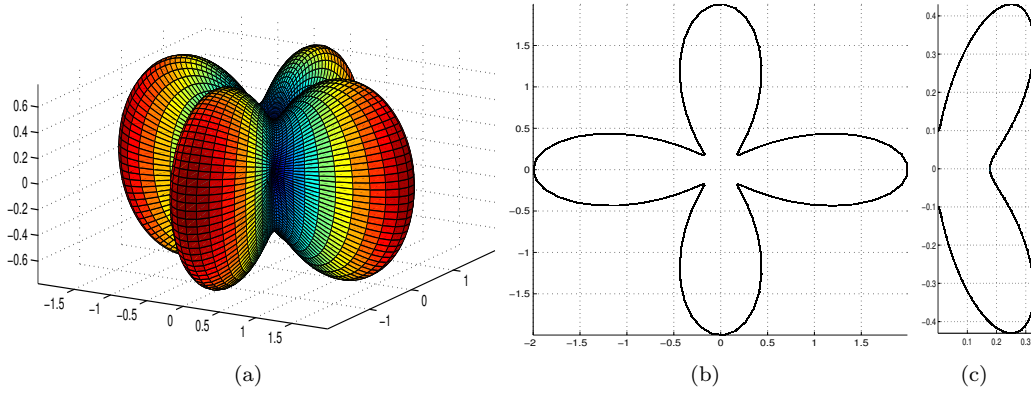


Figure 4. (a) 3-D polar plot along with (b) xy and (c) xz sections in a tetragonal anisotropic system for plate like equilibrium morphology; obtained using $[P^4]'$.

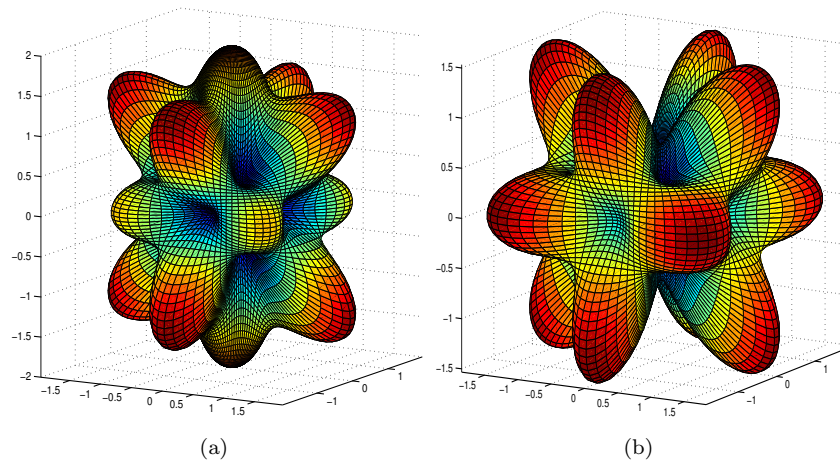


Figure 5. 3-D polar plots in a tetragonal anisotropic system obtained using $[P^6]'$. For (a) the polynomial coefficients are chosen such that both $\langle 100 \rangle$ and $\langle 111 \rangle$ are preferred. For (b) the polynomial coefficients are chosen such that $\langle 100 \rangle$, $\langle 111 \rangle$ and $\langle 001 \rangle$ are preferred.

3. Governing equations and numerical implementation

Once the free energy is given, the variational derivative of the free energy functional with composition gives the relevant chemical potential (μ) [30, 34]:

$$\mu = \frac{\delta F}{\delta c} = \frac{\partial f_0}{\partial c} - \frac{\partial}{\partial x_i} \left[\frac{\partial f}{\partial c_i} \right] + \frac{\partial^2}{\partial x_i \partial x_j} \left[\frac{\partial f}{\partial c_{ij}} \right] - \frac{\partial^3}{\partial x_i \partial x_j \partial x_k} \left[\frac{\partial f}{\partial c_{ijk}} \right], \quad (15)$$

where we have used Einstein summation convention, namely, that repeated indices are summed.

We assume the mobility M to be a constant; incorporating mass conservation (that is, composition is a conserved order parameter), we obtain the Cahn-Hilliard equation which governs concentration changes in such a system:

$$\frac{\partial c}{\partial t} = M \nabla^2 [\mu_0 - \mu_{c_i} + \mu_{c_{ij}} - \mu_{c_{ijk}}] \quad (16)$$

where $\mu_0 = \frac{\partial f_0}{\partial c}$, $\mu_{c_i} = \frac{\partial}{\partial x_i} \left[\frac{\partial f}{\partial c_i} \right]$, $\mu_{c_{ij}} = \frac{\partial^2}{\partial x_i \partial x_j} \left[\frac{\partial f}{\partial c_{ij}} \right]$, and, $\mu_{c_{ijk}} = \frac{\partial^3}{\partial x_i \partial x_j \partial x_k} \left[\frac{\partial f}{\partial c_{ijk}} \right]$. In Table 8, we list these chemical potential terms for each of the polynomials listed in Table 6.

From Table 8, it is clear that the second order polynomials, be in gradient, or curvature or aberration, lead to linear terms in the evolution equation; such evolution equations are solved using semi-implicit Fourier spectral technique [26, 30, 35]. The fourth and sixth order polynomials in gradients lead to highly nonlinear terms in the ECH equation; they are solved using explicit Fourier spectral technique the details of which can be found in [25, 26].

Table 8. The chemical potentials μ_{c_i} , $\mu_{c_{ij}}$ and $\mu_{c_{ijk}}$.

μ	Expression
$\mu_{c_i}(2)$	$2p_1(c_{11} + c_{22}) + 2p_2c_{33}$
$\mu_{c_i}(4)$	$12m_1c_1^2c_{11} + 12m_1c_2^2c_{22} + 16m_2c_1c_2c_{12} + 4m_2c_{11}c_2^2 + 4m_2c_{22}c_1^2 + 12m_3c_3^2c_{33}$ $+ 16m_4c_3(c_1c_{31} + c_2c_{23}) + 4m_4c_{11}c_3^2 + 4m_4c_{22}c_3^2 + 4m_4c_{33}(c_1^2 + c_2^2)$
$\mu_{c_i}(6)$	$6n_1(c_{11} + c_{22})(c_1^2 + c_2^2)^2 + 24n_1(c_1^2 + c_2^2)(c_1c_{11} + 2c_2c_{12} + c_2c_{22}) + 30n_2c_3^4c_{33}$ $+ 12n_3c_1^2c_2^2(c_{11} + c_{22}) + 16n_3c_{12}(c_1^2c_2 + c_1c_2^2) + 2n_3(c_1^4c_{11} + c_1^4c_{22})$ $+ 4n_4c_3^2(c_1^2 + c_2^2)(c_{11} + c_{22}) + 16n_4c_3(c_1^2 + c_2^2)(c_1c_{31} + c_2c_{32}) + 2n_4c_{33}(c_1^2 + c_2^2)^2$ $+ 8n_4c_3^2(c_1c_{11} + 2c_2c_{12} + c_2c_{22}) + 2n_5(c_{11} + c_{22})c_3^4$ $+ 16n_5c_3^3(c_1c_{31} + c_2c_{23}) + 12n_5c_3^2c_{33}(c_1^2 + c_2^2)$ $+ 2n_6(c_{11}c_2^2c_3^2 + c_{22}c_1^2c_3^2 + c_{33}c_1^2c_2^2) + 8n_6(c_1c_2c_{12}c_3^2 + c_1c_3c_{31}c_2^2 + c_2c_3c_{23}c_1^2)$
$\mu_{c_{ij}}$	$2q_1(c_{1111} + c_{2222}) + 2q_2c_{3333} + 4q_3c_{1122} + 4q_4(c_{3311} + c_{2233}) + 2q_5(c_{1313} + c_{2323}) + 2q_6c_{1212}$
$\mu_{c_{ijk}}$	$2r_1(c_{111111} + c_{222222}) + 2r_2c_{333333} + (2r_3 + 2r_{10})(c_{111122} + c_{222211})$ $+ (4r_4 + 8r_6 + 2r_{11})c_{112233} + (4r_5 + 2r_7)(c_{111133} + c_{222233}) + (2r_8 + 4r_9)(c_{333311} + c_{333322})$

The numerical implementation is carried out on the non-dimensionalised evolution equations; the non-dimensionalisation is the same as that described in [30] and leads to a non-dimensional values of unity for the constants A (in the bulk free energy density) and M (mobility); the composition c is scaled to lie between 0 and 1. The far-field composition in the matrix is denoted by c_∞ and is chosen to be 0.2 (in 2-D simulations) and 0.1 (in 3-D simulations). The grid spacing for spatial variables $\Delta x = \Delta y = \Delta z = 0.5$ (in 1- and 2-D simulations) and $\Delta x = \Delta y = \Delta z = 1.0$ (in 3-D

simulations). The time step used in these simulations are $\Delta t = 10^{-5}$ (for P^4 and P^6) and $\Delta t = 10^{-1}$ (for R). The 2-D simulations are carried out on a 256×256 grid while the 3-D simulations are carried out on $100 \times 100 \times 100$ grid. In the next section, at the appropriate places, we list only the independent tensor coefficients (described in Tables. 6 and 8) used in the simulations; the dependent parameters (such as r_{14} for example) are obtained using the relationships listed in Table. 7.

4. Results

In all simulations presented in this section, the a , b and c tetragonal crystallographic axes are aligned with the x , y and z of the simulation cell. We first present the results from 1-D simulations which help us generate the Wulff plots for given anisotropic interfacial free energies; these Wulff plots are consistent with the free energy polar plots shown in the formulation section. Then, we present the 2- and 3-D precipitate morphologies and analyse them using the Wulff construction on the free energy polynomial plot; this analysis is qualitative and shows that our precipitate morphologies obtained during the simulations are indeed equilibrium ones.

4.1. Wulff plots obtained from 1D simulations

Using 1-D simulations of planar interfaces with different interface orientations, the variation of interfacial energy with interface orientation can be plotted – the so-called Wulff plots [36]. As an example, we show results from a set of calculations in which only P^6 tensor coefficient was assumed to be non-zero. We have generated the xy plane section of the Wulff plots for systems that show tetragonal symmetry (specifically, one in which the $\langle 100 \rangle$, $\langle 001 \rangle$ and $\langle 111 \rangle$ directions are preferred). Four-fold xy section perpendicular to $\langle 001 \rangle$ is shown in Fig. 6 (a) and xyz section perpendicular to $\langle 110 \rangle$ is shown in Fig. 6 (b). For (a), we have used $n_1 = 100.0$ and $n_3 = 500.0$ (as only xy -section is considered here), and for (b) we have used $n_1 = 100.0$, $n_2 = 27.0$, $n_3 = 500.0$, $n_4 = 1000.0$, $n_5 = 600.0$ and $n_6 = -5900.0$. In these calculations we fix the components of second rank gradient free energy coefficients (P^2 tensor) at $p_1 = 1.0$ and $p_2 = 0.27$. Similar Wulff plot sections for other planes and for other systems are possible. However, for the sake of brevity, we only show these two in this paper.

4.2. Equilibrium precipitate morphology

In this subsection, we present the equilibrium precipitate morphologies; we start with 2-D results. In tetragonal systems, the xy 2D section is different from the yz 2D section. Of course, the xz 2D section is the same as the yz section. Hence, in 2D, we have carried out simulations for both the cases, namely, xy and yz section. After 2D results, we describe more complex precipitate morphologies in 3-D for different choices of higher order free energy polynomials.

4.2.1. Morphologies in 2D

In Fig. 7 (a) and (b), we show the precipitate morphology after 170 time units using non-zero P^6 – for the xy and yz planes of the tetragonal system respectively. The simulation was started with a circular precipitate of size twelve at the centre of the

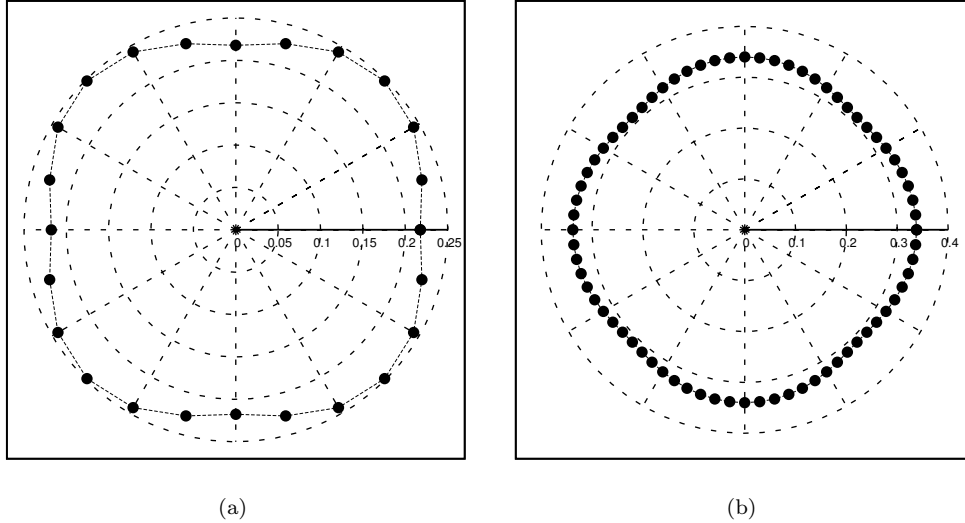


Figure 6. The (a) xy and (b) xyz -sections of the Wulff plot obtained using P^6 .

simulation cell. In the xy plane, tetragonal symmetry leads to four fold symmetry – which is the same as the 2D cubic systems and hence as seen in Fig. 7 (a), the precipitate morphology is squarish. On the other hand, the Fig. 7 (b), which corresponds to the yz plane leads to a lens shaped morphology – by virtue of $a \neq c$ in tetragonal symmetry. The microstructure in Fig. 7 (a) is obtained using $n_1 = 500.0$ and $n_3 = 5000.0$, and in Fig. 7 (b) is obtained using $n_1 = 500.0$, $n_2 = 1200$, $n_4 = 5000$ and $n_5 = 10$. As we show in the next subsection (where 3-D precipitate morphologies are described), for a different choice of parameters, in the yz plane, it is possible to obtain a rectangular morphology (instead of the lens-shape).

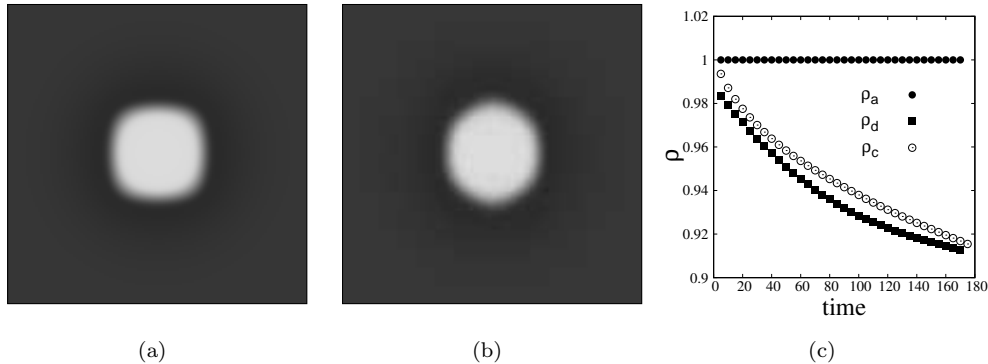


Figure 7. Precipitate morphology obtained using P^6 . (a) represents morphology with facets along x -axis and (b) represents morphology with corners along c -axis. (c) is the aspect ratios (ρ) of these precipitates during the growth.

In Fig. 7 (c), we also show the aspect ratios (ρ) as a function of time. For the precipitate in the xy plane, we have plotted two aspect ratios: ρ_a is the aspect ratio of the size of the precipitate along x axis to that along the y -axis; ρ_d is the aspect ratio of the size of the precipitate along the x axis to that along the diagonal direction (xy direction). As we can see, the ρ_a starts at unity (since our initial precipitate shape is circular) and remains at unity (since the shape evolves into a square); ρ_d which starts

at unity (circular shape) becomes smaller than one – though it does not reach the value of $1/\sqrt{2} = 0.707$ meant for the perfect square. For the precipitate in the yz plane, we define the aspect ratio ρ_c which is the ratio of the size of the precipitate along the y axis to that along the z direction. The ρ_c , again, starts from unity (circular precipitate) and decreases below unity – representing the development of the lens shaped morphology.

4.2.2. Morphologies in 3D

In this section, we present results from our 3D studies. By appropriate choice of the constants in the higher order polynomials, we show that we can obtain precipitates with prism, plate and di-pyramid morphologies, and, their truncated (more complex) variants.

In Fig. 8 (a), (d) and (g), we show the 3-D polar plots for tetragonal prism, plate and di-pyramid morphologies – obtained using P^2 and P^4 (and the other higher order tensor terms are assumed to be zero). Fig. 8 (a) is obtained using $m_1 = 200.0$, $m_2 = 1000.0$, $m_3 = -30.0$, $m_4 = 291.0$, and $p_1 = p_2 = 1$; Fig. 8 (d) is obtained using $m_1 = 200.0$, $m_2 = 10.0$, $m_3 = -90.0$, $m_4 = 100.0$, $p_1 = 2.0$ and $p_2 = 0.1$; Fig. 8 (g) is obtained using $m_1 = 300.0$, $m_2 = 700.0$, $m_3 = 750.0$, $m_4 = 100.0$, $p_1 = 1$ and $p_2 = 2$.

The xy and xz sections of the prism, plate and di-pyramid are shown using blue lines in Fig. 8 (b) and (c); Fig. 8 (e) and (f); and, Fig. 8 (h) and (i), respectively. The Wulff construction on these sections of the free energy polynomial are shown by the red lines; the inner envelope indicating the equilibrium shape in those sections is clearly seen in these plots. However, note that the equilibrium shapes are qualitative in the sense that they are constructed using the free energy polynomial; for quantitative shapes, the same figures have to be constructed using interfacial free energy plots.

In the case of tetragonal prism, a diamond shape is seen on the xy section of the polar plot due to the free energy minima that appear along $\langle 110 \rangle$ directions; on the other hand, the xz section drawn perpendicular to (110) cut plane (see Fig. 8 (c)), shows elongated c -axis with rounded corners. In the case of tetragonal plate also, a diamond shape is seen on the xy section of the polar plot; on the other hand, on xz section (Fig. 8 (f)), the precipitate is rectangular with elongation along the z -axis. Here, we draw the attention of the reader to the fact that in the Wulff shape, x -axis of the figure is along the diagonal and hence is $\sqrt{2}$ times the crystallographic a -axis. This is important in calculating the aspect ratio of the plates. In the case of tetragonal di-pyramid, a squarish shape is seen in the xy section of the polar plot; we can see equilibrium (011) facets in the xz cross section – shown in Fig. 8 (i).

In Fig. 9, the 3-D precipitate morphologies obtained using our numerical simulations are shown. In all these simulations we start with a spherical precipitate of size twelve at the centre of the simulation cell.

The parameters that give rise to the polar plot Fig. 8 (a) lead to tetragonal prism (four fold symmetry in the ab -plane with an elongated c -axis with rounded corners) as seen in Fig. 9 (a) and (b). The morphologies correspond to 300 time units; Fig. 9 (a) is the view from $\langle 001 \rangle$ direction and Fig. 9 (b) is the view from $\langle 100 \rangle$ direction. The parameters that give rise to the polar plot Fig. 8 (d) lead to tetragonal plate (four fold symmetry in the ab -plane with a shortened c -axis) as seen in Fig. 9 (c) and (d). The morphologies correspond to 360 time units; Fig. 9 (c) is the view from $\langle 001 \rangle$ direction and Fig. 9 (d) is the view from $\langle 110 \rangle$ direction. The parameters that give rise to the polar plot Fig. 8 (g) lead to tetragonal di-pyramid (a shape bounded by eight (111) type of planes) as seen in Fig. 9 (e) and (f). The morphologies correspond to 121 time units; Fig. 9 (e) is the view from $\langle 001 \rangle$ direction and Fig. 9 (f) is the view from $\langle 1\bar{1}0 \rangle$

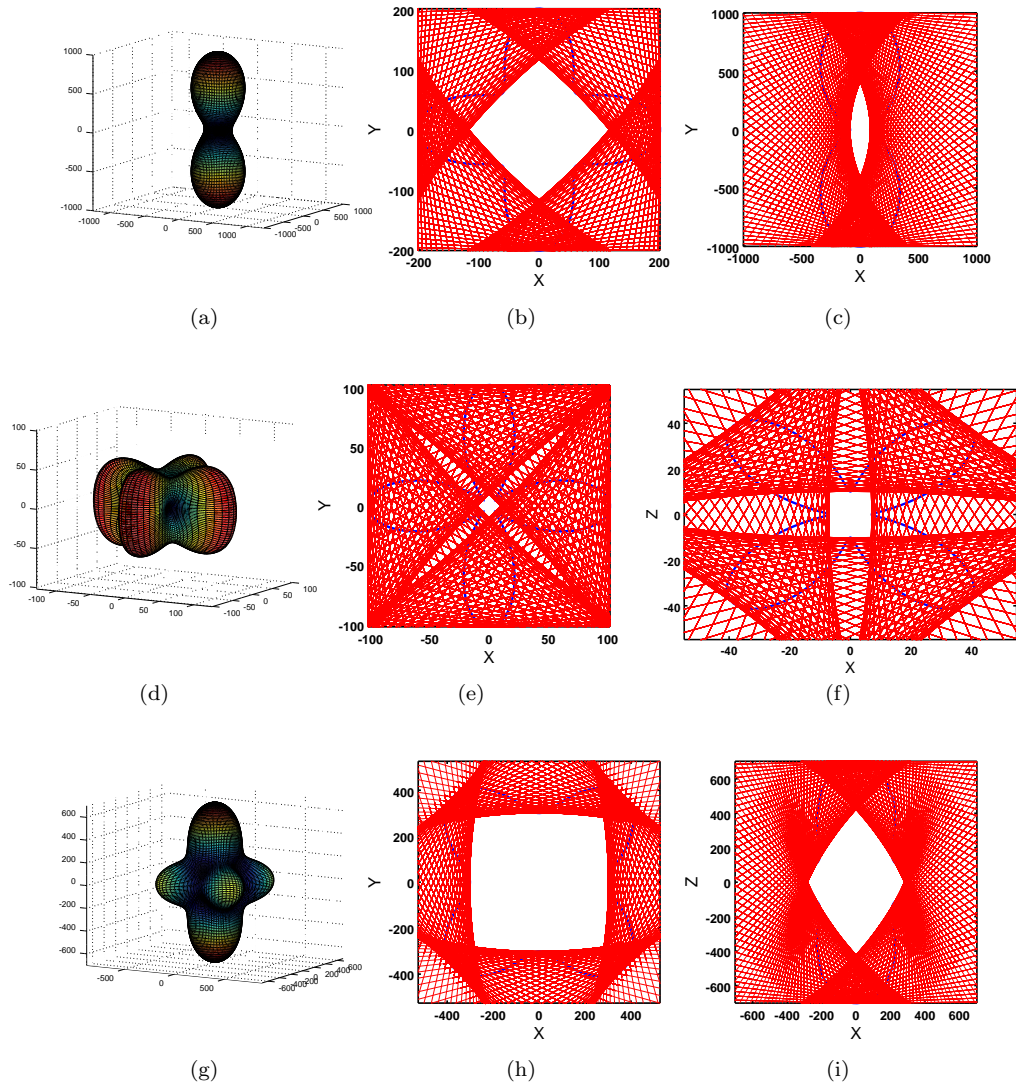


Figure 8. (a) 3-D polar plot and corresponding (b) xy and (c) xz section along with equilibrium Wulff shape for tetragonal prism. (d) 3-D polar plot and corresponding (e) xy and (f) xz section along with equilibrium Wulff shape for tetragonal plate. (g) 3-D polar plot and corresponding (h) xy and (i) xz section along with equilibrium Wulff shape for tetragonal di-pyramid.

direction. Thus, we see that the qualitative Wulff plots obtained by us are consistent with the equilibrium morphologies seen in the simulations.

In order to better understand the 3D morphologies, we calculate and plot the surface normals at the precipitate-matrix interface (by identifying the $c = 0.5$ surface as the interface). In Fig. 10 we present the 3-D surface normal distribution for the prism, plate and di-pyramid ((a), (b) and (c) respectively) for the precipitates shown in Fig. 9. Formation of (110) facets are visible in Fig. 10 (a); we can also see that the planes perpendicular to the c -axes are rounded. Formation of plates (that is, the thickness is small as compared to the dimensions in the ab -plane) with (001) and (110) facets are clearly visible in Fig. 10 (b). The formation of sharp corners and (011) facets can be clearly seen in Fig. 10 (c).

Further characterisation of the morphologies and their evolution during the growth can be achieved using the aspect ratio calculations. Unlike in 2-D and squarish shapes, in these cases (namely, prism, plate and di-pyramids) a large number of aspect ratios can be defined. We have decided to define the following aspect ratios. For all the cases, in the ab -plane (which possesses a four-fold symmetry), we define the aspect ratio ρ as the ratio of size along $\langle 100 \rangle$ to that of $\langle 110 \rangle$ – ρ_{110}^{pl} , ρ_{110}^{pr} and ρ_{110}^{dip} for plate, prism and di-pyramid morphologies respectively. In order to understand the tetragonality of the morphology, we define ρ_{001}^{pl} , ρ_{001}^{pr} and ρ_{001}^{dip} as the ratios of the sizes of the plates, prisms and di-pyramids, respectively, along $\langle 100 \rangle$ to that along $\langle 001 \rangle$.

The aspect ratios (ρ) for morphologies shown in Fig. 9 are shown in Fig. 11. We show the variation of ρ with effective radius R (that is, the radius of a spherical precipitate with the same volume) of the precipitate. In in ab -plane, in the case of plate and prism morphologies $\langle 110 \rangle$ facets form, and, in the case of di-pyramid morphology, $\langle 100 \rangle$ facets form. Hence, both ρ_{110}^{pl} and ρ_{110}^{pr} attain values above unity (namely, 1.182 and 1.169, respectively), while for the di-pyramid morphology, ρ_{001}^{dip} attains a value less than unity (namely, 0.83).

In the case of prism and di-pyramid precipitate morphologies, ρ_{001}^{pr} and ρ_{001}^{dip} attain values less than unity (0.856 for prism and 0.814 for di-pyramid morphology). This is because the precipitate is elongated along c -axis as compared to a - and b -axes. For the plate morphology, ρ_{001}^{pr} attains values greater than unity (1.110). This is because the dimensions in the ab -plane are larger as compared to the thickness of the precipitate.

4.2.3. 3-D equilibrium precipitate morphologies with more than one family of planes

In these systems, there could be precipitate morphologies that consist of two sets of planes, namely, (100) and (111) or morphologies that consists of three sets of planes, namely, {100}, {001} and {111}. These lead to truncated paralleopiped morphologies.

The free energy polynomial assuming that only P^6 and P^2 are non-zero is shown in Fig. 12 (a); specifically, we have used $n_1 = 500.0$, $n_2 = 1200.0$, $n_3 = 5000.1$, $n_4 = 5000.0$, $n_5 = 10.0$, $n_6 = -5000$, $p_1 = 1$ and $p_2 = 2.4$. The xy section, xz section perpendicular to $\langle 100 \rangle$ and the xz section perpendicular to $\langle 110 \rangle$ are shown (in blue) in Fig. 12 (b), (c) and (d), respectively. The red lines are the Wulff construction lines. Even though the Wulff construction on these 2-D sections show that there is minima along $\langle 100 \rangle$, $\langle 011 \rangle$ and $\langle 111 \rangle$ directions, the equilibrium morphology in this system consists only of (100) and (111) facets. This is because the (100) planes have relatively lower energy as compared to (011) planes. Our numerical simulations in which a spherical precipitate of size twelve placed at the centre of the simulation cell, indeed leads to the expected morphology after 250 time units as shown in Fig. 13: (a)

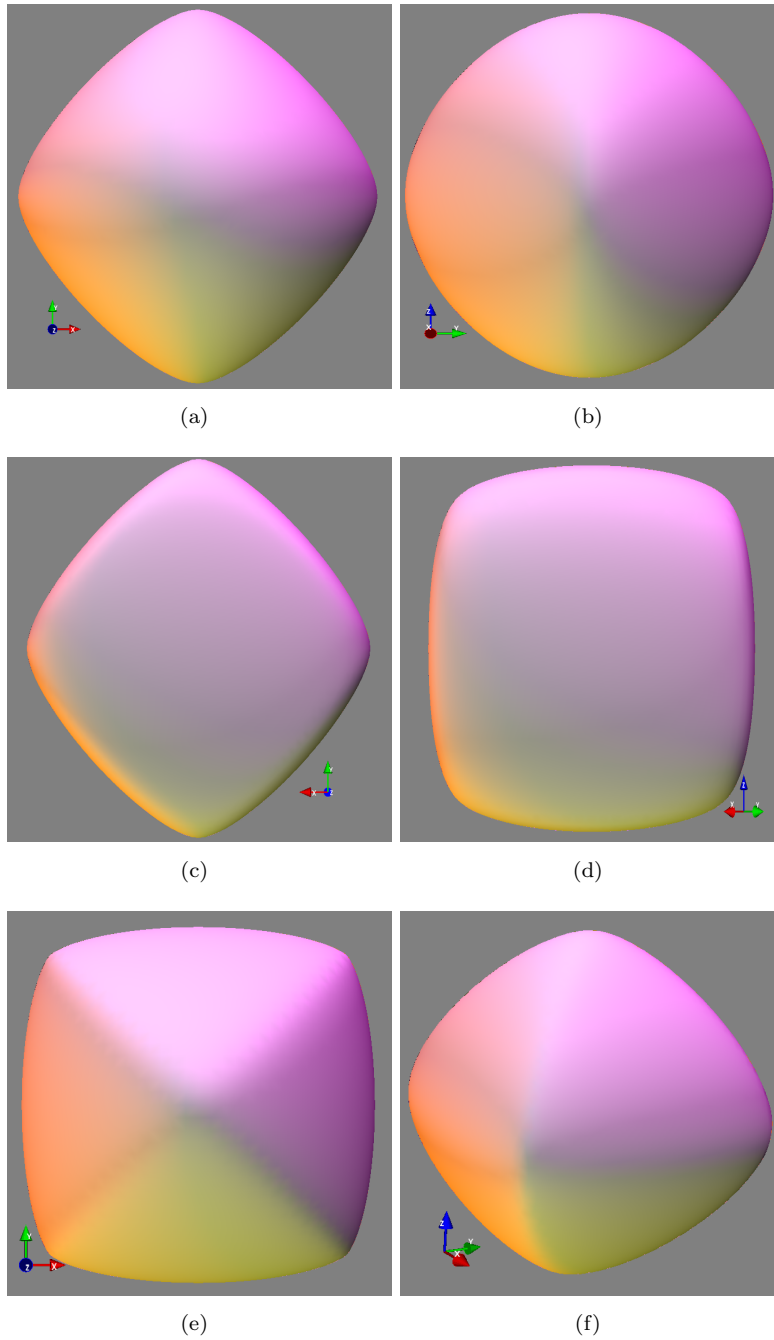


Figure 9. View from (a) $\langle 001 \rangle$ and (b) $\langle 100 \rangle$ directions of a tetragonal prism morphology, from (c) $\langle 001 \rangle$ and (d) $\langle 110 \rangle$ directions of a tetragonal plate morphology, and from (e) $\langle 001 \rangle$ and (f) $\langle 110 \rangle$ directions of a tetragonal di-pyramid morphology.

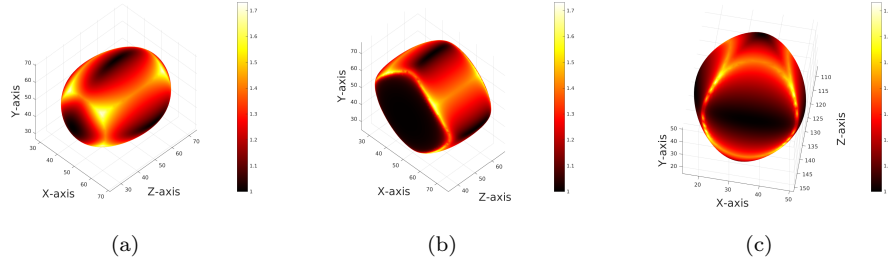


Figure 10. Surface normal distribution – (a) for tetragonal prism morphology; (b) for tetragonal plate morphology; and, for tetragonal di-pyramid morphology.

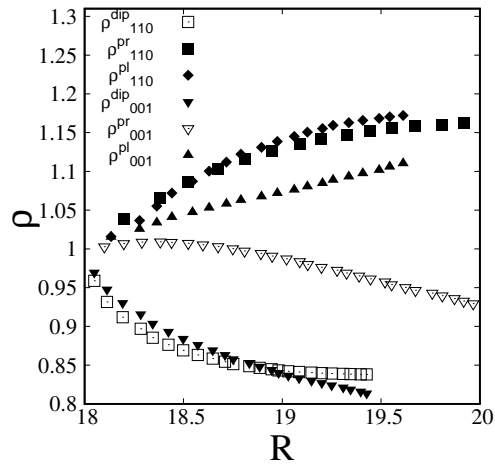


Figure 11. Variation of aspect ratios (ρ) with effective radii for tetragonal precipitate morphologies obtained using P^4 polynomial.

is the view of the precipitate from $\langle 001 \rangle$ and (b) is the view of the precipitate from $\langle 100 \rangle$. The Fig. 13 (c) shows the surface normal plot of this precipitate (generated by identifying the interface at $c = 0.5$); the colour bar indicates $\sqrt{h^2 + k^2 + l^2}$ for $\langle hkl \rangle$ orientation. So, a numerical value of 1.0, 1.414 and 1.732 represent the planes containing $\langle 100 \rangle$, $\langle 110 \rangle$ and $\langle 111 \rangle$ directions respectively. Note that the surface normal plot also shows that $\langle 001 \rangle$ planes are missing in this morphology.

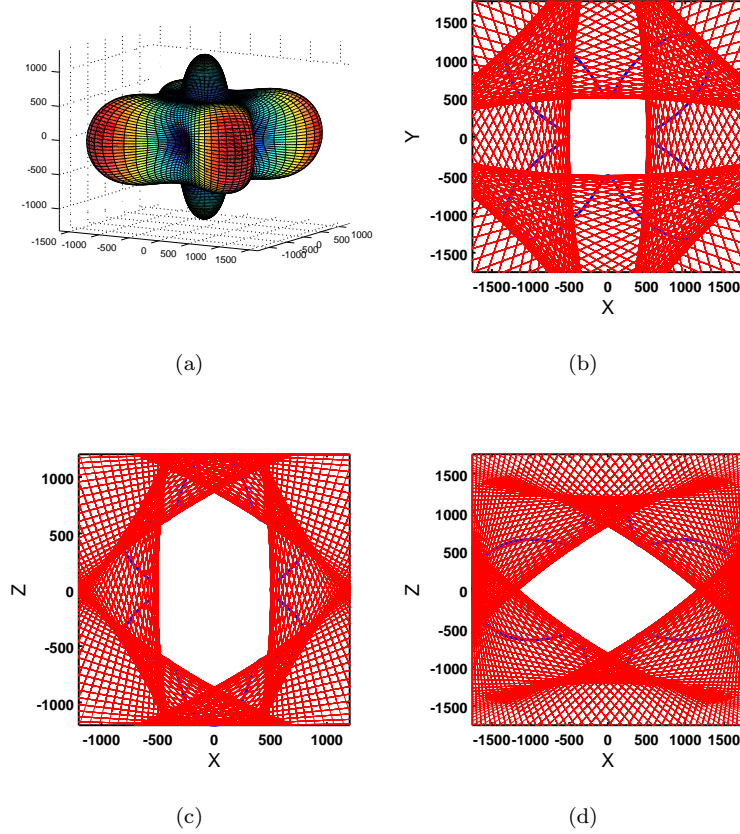


Figure 12. Morphology with two types of facets obtained using P^6 : (a) 3-D polar plot; (b) xy section (at the centre), and xz section (at the centre) perpendicular to (c) $\langle 100 \rangle$ and (d) $\langle 110 \rangle$ directions; in all the 2D sections, the Wulff constructions are also shown.

If the parameters are chosen as $n_1 = 100.0$, $n_2 = 27.0$, $n_3 = 500.0$, $n_4 = 1000.0$, $n_5 = 600$, $n_6 = -5900.0$, $p_1 = 1$ and $p_2 = 0.27$, the resultant free energy polynomial is as shown in Fig. 14. From this polar plot as well as the Wulff construction on the 2-D sections (xy and xz -sections perpendicular to $\langle 100 \rangle$ and $\langle 110 \rangle$), it is clear that in this case, in addition to $\langle 100 \rangle$ and $\langle 111 \rangle$ planes, $\langle 001 \rangle$ planes are also expected to form. The morphology obtained from numerical simulations of a precipitate of size twelve placed at the centre of the simulation cell and evolved to 360 time units is shown in Fig. 15: (a) is the view of the precipitate from $\langle 001 \rangle$ and (b) is the view of the precipitate from $\langle 111 \rangle$. From these figures as well as the surface normal plot shown in Fig. 15 (c), it is clear that this morphology does consist of three families of planes – $\langle 100 \rangle$, $\langle 001 \rangle$ and $\langle 111 \rangle$.

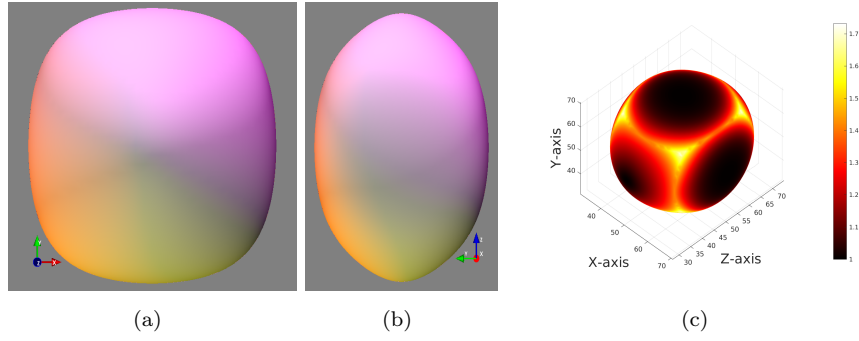


Figure 13. View from (a) $\langle 001 \rangle$ and (b) $\langle 100 \rangle$ of a precipitate with two types of facets obtained by incorporating sixth-rank gradient tensor coefficients. The surface normal distribution for the morphology is shown in (c).

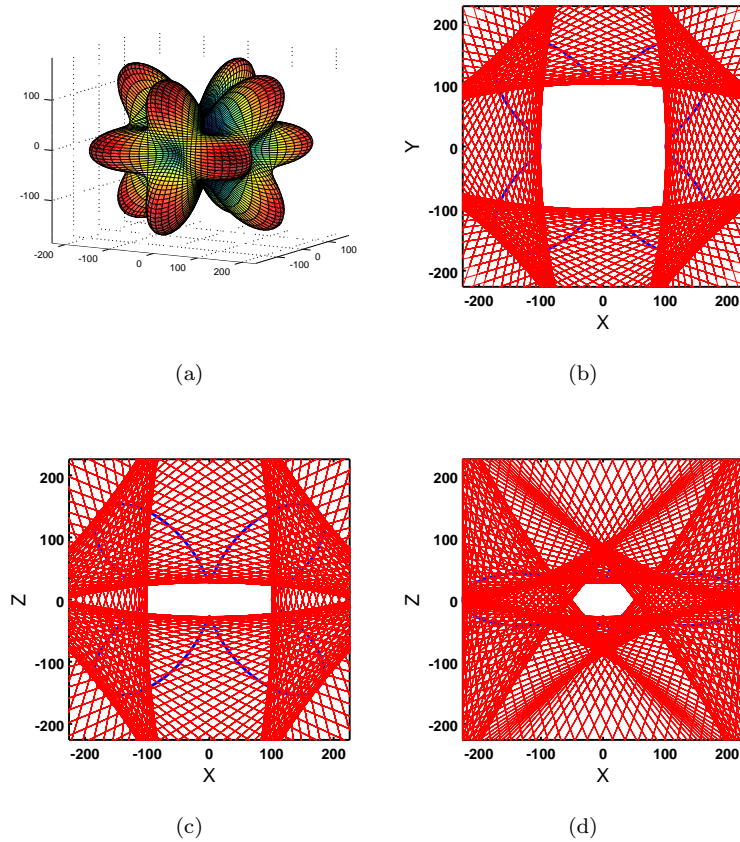


Figure 14. Morphology with three types of facets obtained using P^6 : (a) 3-D polar plot; (b) xy section (at the center); xz sections perpendicular to (c) $\langle 100 \rangle$ and (d) $\langle 110 \rangle$ directions. The Wulff constructions are also shown in all the 2-D sections.

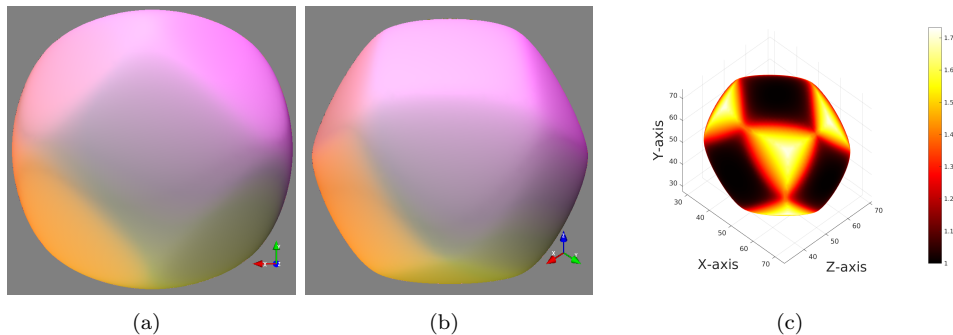


Figure 15. Tetragonal morphology with three facets obtained using sixth-rank gradient tensor terms. (a) represents a view from $\langle 001 \rangle$ direction and (b) represents a view from $\langle 111 \rangle$ direction. The surface normal distribution for the prism morphology is shown in (c).

5. Conclusions

A wide variety of morphologies are observed in technologically important tetragonal systems (such as TiO_2 and Sn, for example). We have developed a family of Extended Cahn-Hilliard (ECH) models for systems of tetragonal interfacial free energy anisotropy; we have identified the non-zero and independent constants that enter the model (for fourth and sixth rank tensors) of gradient, curvature and aberration terms as well as the constraints on these. We have numerically implemented the ECH model; and, we show that by appropriate choice of constants, using our numerical implementation, it is possible to obtain prisms, plates, di-pyramids and their truncated variants (with two or three different crystallographic planes bounding the precipitate). Our formulation leads to precipitate morphologies that are consistent with the Wulff construction. We have characterised the precipitate morphologies using aspect ratios and surface normal plots. It is possible to extend our model by incorporating elastic stress effects and we believe that such an extension will lead to interesting insights in morphological evolution during solid-solid phase transformations in tetragonal systems.

Acknowledgements

We thank Industrial Research and Consultancy Centre, IIT Bombay for financial support (09IRCC16); and, PARAM-YUVA at CDAC, Pune, Nebula, Dendrite (DST-FIST HPC facility), Spinode, and Leopard, GPU Centre of Excellence (GCoE), IIT Bombay for computational facilities. One of us (AR) thank DST for partial financial support (14DST017).

References

- [1] G. Liu, J.C. Yu, G.Q.M. Lu, and H.M. Cheng, *Crystal facet engineering of semiconductor photocatalysts: motivations, advances and unique properties.*, Chem. Commun. 47 (2011), pp. 6763–83.
- [2] M. Egashira, T. Matsumoto, Y. Shimizu, and H. Iwanaga, *Gas-sensing characteristics of tin oxide whiskers with different morphologies*, Sensor. Actuator. 14 (1988), pp. 205–213.
- [3] V. Lanteri, T.E. Mitchell, and A.H. Heuer, *Morphology of Tetragonal Precipitates in Partially Stabilized ZrO_2* , J. Am. Ceram. Soc. 69 (1986), pp. 564–569.

- [4] P.J. Othen, M.L. Jenkins, and G.D.W. Smith, *High-resolution electron microscopy studies of the structure of Cu precipitates in α -Fe*, Philos. Mag. A 70 (1994), pp. 1–24.
- [5] R. Monzen, K. Takada, and C. Watanabe, *Coarsening of Spherical Cu Particles in an α -Fe matrix*, ISIJ Int. 44 (2004), pp. 442–444.
- [6] R. Ravelo and M. Baskes, *Equilibrium and Thermodynamic Properties of Grey, White, and Liquid Tin*, Phys. Rev. Lett. 79 (1997), pp. 2482–2485.
- [7] W.J. Boettinger, C.E. Johnson, L.A. Bendersky, K.W. Moon, M.E. Williams, and G.R. Stafford, *Whisker and Hillock formation on Sn, Sn-Cu and Sn-Pb electrodeposits*, Acta Mater. 53 (2005), pp. 5033–5050.
- [8] M. Sobiech, U. Welzel, E.J. Mittemeijer, W. Hugel, and A. Seekamp, *Driving force for Sn whisker growth in the system Cu-Sn*, Appl. Phys. Lett. 93 (2008), pp. 21–24.
- [9] M. Chen and L.D. Schmidt, *Morphology and composition of PtPd alloy crystallites on SiO₂ in reactive atmospheres*, J. Catal. 56 (1979), pp. 198–218.
- [10] Y. Deng, J.L. Wang, K.R. Zhu, M.S. Zhang, J.M. Hong, Q.R. Gu, and Z. Yin, *Synthesis and characterization of single-crystal PbTiO₃ nanorods*, Mater. Lett. 59 (2005), pp. 3272–3275.
- [11] A.R. Wang and H. Xiao, *Controllable preparation of SnO₂ nanoplates and nanoparticles via hydrothermal oxidation of SnS₂ nanoplates*, Mater. Lett. 63 (2009), pp. 1221–1223.
- [12] H. Uchiyama, H. Ohgi, and H. Imai, *Selective preparation of SnO₂ and SnO crystals with controlled morphologies in an aqueous solution system*, Cryst. Growth Des. 6 (2006), pp. 2186–2190.
- [13] G. Saito, S. Hosokai, M. Tsubota, and T. Akiyama, *Influence of solution temperature and surfactants on morphologies of tin oxide produced using a solution plasma technique*, Cryst. Growth Des. 12 (2012), pp. 2455–2459.
- [14] K.N. Tu and J.C.M. Li, *Spontaneous whisker growth on lead-free solder finishes*, Mat. Sci. Eng. A 409 (2005), pp. 131–139.
- [15] J.C. Heyraud and J.J. Metois, *Surface free energy anisotropy measurement of indium*, Surf. Sci. 177 (1986), pp. 213 – 220.
- [16] T. Yanagihara, *Equilibrium Shape of Indium Particles*, Jpn. J. Appl. Phys. 21 (1982), pp. 1554 – 1558.
- [17] J. Luo, H.T. Zhu, H.M. Fan, J.K. Liang, H.L. Shi, G.H. Rao, J.B. Li, Z.M. Du, and Z.X. Shen, *Synthesis of single-crystal tetragonal α -MnO₂ nanotubes*, J. Phys. Chem. C 112 (2008), pp. 12594–12598.
- [18] K. Kaneko, K. Inoke, B. Freitag, A.B. Hungria, P.A. Midgley, T.W. Hansen, J. Zhang, S. Ohara, and T. Adschiri, *Structural and morphological characterization of cerium oxide nanocrystals prepared by hydrothermal synthesis*, Nano Lett. 7 (2007), pp. 421–425.
- [19] A.S. Barnard, P. Zapol, and L.A. Curtiss, *Modeling the morphology and phase stability of TiO₂ nanocrystals in water*, J. Chem. Theory Comput. 1 (2005), pp. 107–116.
- [20] B. Liu and E.S. Aydil, *Growth of oriented single-crystalline rutile TiO₂ nanorods on transparent conducting substrates for dye-sensitized solar cells*, J. Am. Chem. Soc. 131 (2009), pp. 3985–3990.
- [21] W. Yang, Y. Wang, and W. Shi, *One-step synthesis of single-crystal anatase TiO₂ tetragonal faceted-nanorods for improved-performance dye-sensitized solar cells*, CrystEngComm 14 (2012), pp. 230–234.
- [22] R. Kikuchi and J.W. Cahn, *Theory of domain walls in ordered structures-II Pair approximation for nonzero temperatures*, J. Phys. Chem. Solids 23 (1962), pp. 137–151.
- [23] R. Kikuchi and J.W. Cahn, *Theory of interphase and antiphase boundaries in f.c.c. alloys*, Acta Metall. Mater. 27 (1979), pp. 1337–1353.
- [24] E.S. Nani and M.P. Gururajan, *On the incorporation of cubic and hexagonal interfacial energy anisotropy in phase field models using higher order tensor terms*, Philos. Mag. 94 (2014), pp. 3331–3352.
- [25] A. Roy, E.S. Nani, A. Lahiri, and M.P. Gururajan, *Interfacial free energy anisotropy driven faceting of precipitates*, preprint (2017), to appear in Philos. Mag. Available at <https://doi.org/10.1080/14786435.2017.1348633>.

- [26] A. Roy, *Effect of energetic and kinetic interfacial anisotropies on microstructures: a phase field study*, Unpublished doctoral dissertation, Indian Institute of Technology Bombay, Mumbai, INDIA, 2017.
- [27] R.J. Braun, J.W. Cahn, G.B. McFadden, and A.A. Wheeler, *Anisotropy of interfaces in an ordered alloy: A multiple-order-parameter model*, Philos. T. Roy. Soc. A 355 (1997), pp. 1787–1833.
- [28] Y. Wang, D. Banerjee, C.C. Su, and A.G. Khachaturyan, *Field kinetic model and computer simulation of precipitation of $L1_2$ ordered intermetallics from f.c.c. solid solution*, Acta Mater. 46 (1998), pp. 2983–3001.
- [29] V. Vaithyanathan, C. Wolverton, and L.Q. Chen, *Multiscale modeling of precipitate microstructure evolution.*, Phys. Rev. Lett. 88 (2002), p. 125503.
- [30] T.A. Abinandanan and F. Haider, *An extended Cahn-Hilliard model for interfaces with cubic anisotropy*, Philos. Mag. A 81 (2001), pp. 2457–2479.
- [31] S. Torabi and J. Lowengrub, *Simulating interfacial anisotropy in thin-film growth using an extended Cahn-Hilliard model*, Phys. Rev. E 85 (2012), pp. 041603–16.
- [32] J.F. Nye, *Physical properties of crystals: their representation by tensors and matrices*, Oxford science publications, Clarendon Press, Oxford, 1985.
- [33] G.F. Smith, M.M. Smith, and R.S. Rivlin, *Integrity bases for a symmetric tensor and a vector – the crystal classes*, Arch. Ration. Mech. An. 12 (1963), pp. 93–133.
- [34] I.H. Shames and C.L. Dym, *Energy and Finite Element Methods in Structural Mechanics*, New Age International, New Delhi, 1995.
- [35] L.Q. Chen and J. Shen, *Applications of semi-implicit Fourier-spectral method to phase field equations*, Comput. Phys. Commun. 108 (1998), pp. 147–158.
- [36] D.A. Porter and K.E. Easterling, *Phase transformations in metals and alloys*, Chapman & Hall, London, 1996.